

# Regular and chaotic dynamics in 3D reconnecting current sheets

C. Gontikakis,<sup>1\*</sup> C. Efthymiopoulos<sup>1\*</sup> and A. Anastasiadis<sup>2\*</sup>

<sup>1</sup>*Academy of Athens, Research Centre of Astronomy and Applied Mathematics, Soranou Efessiou 4, GR-11527 Athens, Greece*

<sup>2</sup>*National Observatory of Athens, Institute for Space Applications and Remote Sensing GR-15236, Penteli, Greece*

Accepted 2006 January 20. Received 2006 January 13; in original form 2005 December 13

## ABSTRACT

We consider the possibility of particles being injected at the interior of a reconnecting current sheet (RCS), and study their orbits by dynamical systems methods. As an example we consider orbits in a 3D Harris type RCS. We find that, despite the presence of a strong electric field, a ‘mirror’ trapping effect persists, to a certain extent, for orbits with appropriate initial conditions within the sheet. The mirror effect is stronger for electrons than for protons. In summary, three types of orbits are distinguished: (i) chaotic orbits leading to escape by stochastic acceleration, (ii) regular orbits leading to escape along the field lines of the reconnecting magnetic component, and (iii) mirror-type regular orbits that are trapped in the sheet, making mirror oscillations. Dynamically, the latter orbits lie on a set of invariant KAM tori that occupy a considerable amount of the phase space of the motion of the particles. We also observe the phenomenon of ‘stickiness’, namely chaotic orbits that remain trapped in the sheet for a considerable time. A trapping domain, related to the boundary of mirror motions in velocity space, is calculated analytically. Analytical formulae are derived for the kinetic energy gain in regular or chaotic escaping orbits. The analytical results are compared with numerical simulations.

**Key words:** acceleration of particles – Sun: flares.

## 1 INTRODUCTION

Magnetic reconnection is the term used to describe a collection of phenomena that take place when magnetic fields with opposite orientation, carried by a hot plasma, come close together within a very small volume of space. Theoretical models of reconnection (see Priest & Forbes 2000 for a review) typically predict the formation, within the reconnecting topology, of reconnecting current sheets (RCS). A simple RCS model is shown in Fig. 1. Plasma is flowing into the sheet from two opposite directions (see arrows), and the plasma is forced to flow out of the sheet in the direction indicated by a third arrow. The plasma carries magnetic lines with it, so that there is a constant Poynting flux established through the sheet. If  $v$  is the typical inflow velocity, there is an electric field seen in the rest frame which, ignoring a Lorentz factor, is given by  $E = -v \times B$ , where  $B$  is the reconnecting magnetic field component. The effects of oppositely oriented magnetic fields and inflow directions mutually cancel each other out, so that  $E$  has the same orientation on both sides of the sheet. This roughly constant electric field acts as an accelerator for the charged particles of the plasma. If the electric field is strong enough, the motions of energetic particles become effectively collisionless, thus they can be studied by orbital theory. These conditions are quite common in a number of astrophysical contexts. Well known examples are current sheets formed

in the Earth’s magnetotail (Speiser 1965) and in the solar atmosphere (Somov 1992).

When the electric field is strong, particles are accelerated by the electric field as soon as they enter into the sheet at its edges. Such particles cannot be trapped in the sheet; they escape, usually gaining considerable amounts of kinetic energy within very small times compared to the RCS lifetime. For example, it is estimated that in solar flare conditions electrons gain hundreds of keVs within  $10^{-6}$  s, while ions gain tens of MeV within  $10^{-3}$  s. The effectiveness of a RCS as an accelerator depends on a number of parameters related to the RCS geometry (e.g. X-type, spine) or the initial conditions of the particles when they are injected (see Aschwanden 2004, for a review). This has been a subject of intense research mostly by solar, plasma or geo-physicists. Indicative references are Speiser (1965), Cowley (1978), Bulanov (1980), Speiser & Lyons (1984), Chen & Palmadesso (1986), Martens (1988), Büchner & Zelenyi (1989, 1991), Martens & Young (1990), Burkhardt, Drake & Chen (1990), Deeg, Borovsky & Duric (1991), Bruhwiler & Zweibel (1992), Chen (1992), Moses, Finn & Ling (1993), Litvinenko & Somov (1993), Zhu & Parks (1993), Litvinenko (1996), Vekstein & Browning (1997), Browning & Vekstein (2001), Dalla & Browning (2005) and Zharkova & Gordovskyy (2004, 2005).

The study of the acceleration problem is complicated by the fact that regions of intense magnetic activity (e.g. in the solar atmosphere) are characterized by the formation of complex RCS structures involving multiple scattering events of the particles that cross them. The complexity of the acceleration process

\*E-mail: cgontik@cc.uoa.gr; cefthim@cc.uoa.gr; anastasi@space.noa.gr

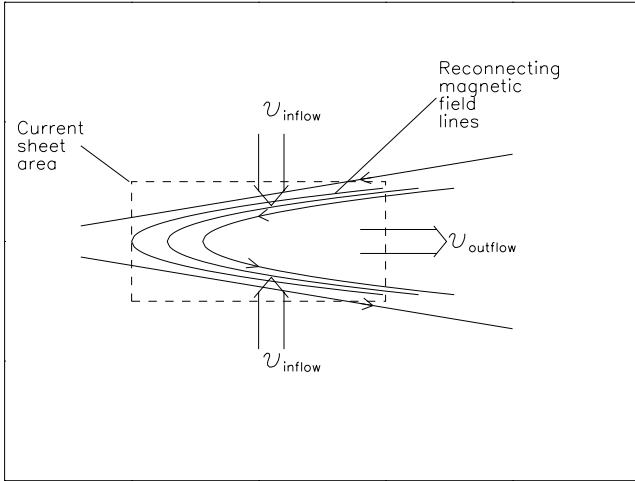


**Figure 1.** A schematic representation of a current sheet showing the inflow and outflow directions of plasma carrying magnetic flux, in and out of the reconnecting region.

notwithstanding, models of multiple scattering events, which use as *input* the dynamics provided by one single RCS (e.g. Anastasiadis, Vlahos & Georgoulis 1997; Anastasiadis et al. 2004), have given results promising enough to justify the study of dynamics in simple RCS configurations.

In a previous paper (Efthymiopoulos, Gontikakis & Anastasiadis 2005, hereafter Paper I) we examined in detail the orbits of accelerated particles in a model Harris-type configuration, for field parameters relevant to RCSs in the solar atmosphere. Our study was based on equations derived analytically by dynamical system methods. Furthermore, we focussed on orbits corresponding to the case of particles entering and leaving the sheet at its edges. Such orbits are representative of a normal flow of plasma through the sheet.

In the present paper we examine a different possibility: particles with initial conditions in the *interior* of the sheet. There are various source mechanisms, besides the sheet plasma itself, that could account for the origin of such a population. For example, consider a ‘breathing’ RCS, in which there are temporary reversals of the flow directions shown in Fig. 1. Such a case is likely, e.g., on top of a coronal loop; namely, the RCS may undergo back and forth fluctuations caused by motions of the loop footpoints that affect the whole geometry of magnetic field lines along the loop. Now, in a phase of reversal of the flow directions of Fig. 1, plasma enters the sheet towards its centre. If, later, the normal flow directions are re-established, a population of particles will be left in the interior of the sheet. A second example is an impulsive event leading to the quick formation of an RCS before particles have time to escape the reconnecting region (Bhattacharjee 2004). These and other situations may lead to populations of particles with initial conditions in the interior of the sheet. The orbits of such particles are the subject of the present paper.

A number of authors have addressed the question of how will *distributions* of particles with initial conditions in the interior of a RCS evolve when acted upon by the RCS force fields (Kliem 1994; Fletcher & Petkaki 1997; Petkaki & MacKinnon 1997; Mori, Sakai & Zhao 1998; Heerikhuisen, Litvinenko & Craig 2002; Nodes et al. 2003; Hamilton et al. 2003). Most of these studies rely on numerical simulations for large ensembles of orbits. In the present paper, beside presenting numerical simulations, our purpose is to develop

an approximate analytical theory that describes these orbits. In particular, we seek to determine the boundary of the domain in velocity space separating escaping from non-escaping orbits. In the absence of electric field, this boundary becomes topologically equivalent to what is referred to as a ‘loss cone’ in the plasma literature. We should stress that the orbits in our model system are, in general, beyond the limits of the guiding centre approximation, hence, the determination of the trapping domain does not follow trivially from the preservation of the first-order adiabatic invariant. Furthermore, in the case of escaping orbits, we find analytical formulae relating the kinetic energy gain as a function of the initial kinetic energy and of the physical parameters of the sheet.

One relevant aspect of our study concerns the separation of particles in those following regular or chaotic orbits. This separation has remarkable dynamical implications. In particular, we find that the orbits inside the trapping domain are mostly regular and lie on manifolds of phase space known as ‘KAM tori’ in dynamical systems theory. However, there are also some chaotic orbits inside the trapping domain. These practically remain trapped in the sheet for very long times. We explain this phenomenon as a ‘stickiness effect’ (see Contopoulos 2002, for a review of stickiness). Finally we find that escaping orbits are either regular or chaotic, but the gain of kinetic energy, as a function of the physical parameters of the sheet and of the initial energy of the particle, scales differently for particles escaping along regular or chaotic orbits.

The paper is structured as follows: Section 2 presents the model used, the Hamiltonian formalism of the equations of motion and the choice of parameter values. Section 3 presents numerical simulations of particle orbits, indicating the separation of the domains of the trapping and escapes. Section 4 is devoted to a theoretical analysis of the orbits by a Hamiltonian formalism, and to a comparison of theoretical with numerical results. Section 5 summarizes the main conclusions of the present study.

## 2 THE MODEL

Our model current sheet configuration is the same as in Litvinenko & Somov (1993). The magnetic and electric fields are (Fig. 2):

$$\begin{aligned} \mathbf{E} &= (0, 0, E) \\ \mathbf{B} &= (-y/a, \xi_{\perp}, \xi_{\parallel})B_0 \quad \text{for } |y| \leq a \\ \mathbf{B} &= [-\text{sgn}(y), \xi_{\perp}, \xi_{\parallel}]B_0 \quad \text{for } |y| > a \end{aligned} \quad (1)$$

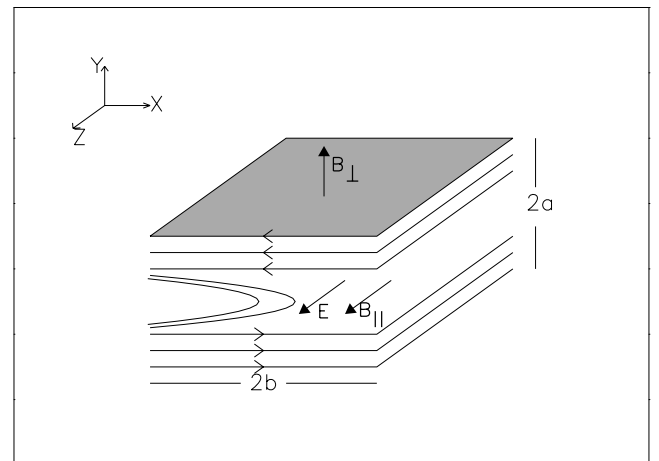


**Figure 2.** The topology of the magnetic and electric fields in the model current sheet.

where  $B_0$  is a typical measure of the magnetic field in a reconnecting region,  $\xi_\perp$ ,  $\xi_\parallel$  and  $E$  are constants, and  $\text{sgn}(y) = y/|y|$ . Equations (1) approximate the Harris configuration  $B_x = B_0 \tanh(y/a)$ , where  $a$  is the half width of the RCS. They also approximate one side of an X-type current sheet. An orbit is integrated up to the moment when it crosses the value  $|y| = a$ , where the orbit is considered as escaping the sheet.

For  $|y| \gg a$  the projections of the magnetic field lines on the  $(x, y)$  plane become almost parallel to the  $x$ -axis, but they are described in opposite senses for  $y > 0$  and  $y < 0$ . On the other hand, the value of the magnetic field in the  $z$ -axis is determined by the parameter  $\xi_\parallel$ . In particular, the relative angle between the upper and lower reconnecting lines is given by  $\tan \phi = \xi_\parallel$ , so that  $\xi_\parallel$  measures the shear of the reconnecting field. In solar RCSs  $\xi_\parallel$  may have any value from zero to as large as the main reconnecting component ( $0 \leq \xi_\parallel \leq 1$ ). In the geomagnetic tail we adopt a shear of  $\xi_\parallel = 0.2$  (see Zhu & Parks 1993, Lee et al. 2001).

For a particle with mass  $m$  and positive charge  $q$ , the non-relativistic equations of motion can be written in dimensionless form:

$$\frac{d^2x}{dt^2} = \xi_\parallel \frac{dy}{dt} - \xi_\perp \frac{dz}{dt} \quad (2)$$

$$\frac{d^2y}{dt^2} = -\xi_\parallel \frac{dx}{dt} - y \frac{dz}{dt} \quad (3)$$

$$\frac{d^2z}{dt^2} = \epsilon + \xi_\perp \frac{dx}{dt} + y \frac{dy}{dt} \quad (4)$$

In these equations the dimensionless electric field is given by  $\epsilon = mE/(aqB_0^2)$ . For negative charge, the same equations hold with either the orientation of the  $y$ - and  $z$ -axes reversed, or the orientation of the magnetic and electric fields reversed. Non-linear terms are introduced by the dependence of the measure of the reconnecting component of the magnetic field,  $B_x$ , on  $y$ .

In equations (2), (3) and (4), the physical quantities are represented by dimensionless parameters. The constants  $\xi_\parallel$  and  $\xi_\perp$  are scaled to the mean value of the magnetic field, as indicated in equation (1). The unit of time is the inverse of the Larmor frequency  $\langle t \rangle = \omega_B^{-1} = m/(qB_0)$ . The length unit,  $\langle L \rangle$ , is set equal to the half thickness,  $a$ , of the current sheet and the electric field unit is given by  $\langle \epsilon \rangle = aB_0^2 q/m$ . All units and parameter values used in our examples below are ensembled in Table 1. The parameter values for RCSs originate from Martens & Young (1990).

The equations of motion (2), (3) and (4) can be derived from a 3-d.o.f. autonomous Hamiltonian function,

$$H = \frac{1}{2}(p_x + \xi_\parallel y)^2 + \frac{1}{2}p_y^2 + \frac{1}{2}\left(p_z + \xi_\perp x + \frac{1}{2}y^2\right)^2 - \epsilon z, \quad (5)$$

where the canonical momenta  $p_x$ ,  $p_y$ ,  $p_z$  are given by the sum of the velocity and of the vector potential components:

$$p_x = \dot{x} - \xi_\parallel y,$$

$$p_y = \dot{y},$$

$$p_z = \dot{z} - \xi_\perp x - \frac{1}{2}y^2. \quad (6)$$

Hamilton's equations

$$\dot{x} = \frac{\partial H}{\partial p_x}, \quad \dot{p}_x = -\frac{\partial H}{\partial x} \quad (7)$$

**Table 1.** The first part shows typical values for the physical parameters of RCSs in solar flares (left-hand column) and in the Earth magnetotail (second column). The second part shows the units and the third part shows the range of parameters used in our computations.

	Solar flares	Earth magnetotail
Estimated values from data		
Magnetic field (Gauss)	100	$2 \times 10^{-4}$
half-thickness (m)	1	$2 \times 10^6$
electric field ( $\text{V m}^{-1}$ )	100	$2.5 \times 10^{-4}$
Gyroradius (el. <sup>1</sup> ) (m)	$3.5 \times 10^{-2}$	$6.8 \times 10^3$
Gyroradius (pr. <sup>1</sup> ) (m)	1.5	$2.9 \times 10^5$
Units		
Magnetic field (Gauss)	100	$2 \times 10^{-4}$
Electric field (el.)( $\text{V m}^{-1}$ )	$10^7$	$1.39 \times 10^2$
Electric field (pr.)( $\text{V m}^{-1}$ )	$5.56 \times 10^3$	$7.5 \times 10^{-2}$
time (el.) (s)	$5.7 \times 10^{-10}$	$0.284 \times 10^{-3}$
time (pr.) (s)	$1.04 \times 10^{-6}$	0.52
length unit (m)	0.58	$2 \times 10^6$
velocity (el.) ( $\text{m s}^{-1}$ )	$1 \times 10^9$	$7 \times 10^9$
velocity (pr.) ( $\text{m s}^{-1}$ )	$0.5 \times 10^6$	$3.8 \times 10^6$
K. energy (el.) (keV)	$5.9 \times 10^3$	$273 \times 10^3$
K. energy (pr.) (keV)	3.22	149
Dimensionless parameters		
$\xi_\perp$	$10^{-3}$	0.05
$\xi_\parallel$	0–1	0.2
$\epsilon$ (el.)	$10^{-5}$	$1.8 \times 10^{-6}$
$\epsilon$ (pr.)	$1.84 \times 10^{-2}$	$3.3 \times 10^{-3}$
sheet half-thickness $a$	1	1

<sup>1</sup>For five times the thermal velocity, computed at  $T = 10^7$  K for solar flare and at  $5.6 \times 10^6$  K for the Earth magnetotail.

(and similarly for  $y$ ,  $p_y$  and  $z$ ,  $p_z$ ), lead to the equations of motion (2), (3) and (4). Furthermore, the Hamiltonian equations admit an exact second integral of motion, independent of and in involution with the Hamiltonian equation (5). The second integral reads

$$I_2 = p_x + \xi_\perp z \quad (8)$$

and one verifies immediately that  $\dot{I}_2 = \{I_2, H\} = 0$ , where  $\{\dots, \dots\}$  stands for the Poisson bracket operator. The existence of a second integral,  $I_2$ , linear in the momentum  $p_x$  allows one to reduce the number of degrees of freedom by one, while keeping the Hamiltonian character of the equations of motion. Following the procedure described in Arnold & Novikov (1995) we find the 2-d.o.f. Hamiltonian:

$$H = \frac{1}{2}p_y^2 + \frac{1}{2}\left(c_4 + \frac{1}{2}y^2\right)^2 + \frac{1}{2}(I_2 - \xi_\perp z + \xi_\parallel y)^2 - \epsilon z, \quad (9)$$

where  $c_4 = \xi_\perp x + p_z$ . The new canonically conjugate pairs are  $(y, p_y)$  and  $(z, c_4)$ . The new Hamilton's equations read

$$\dot{y} = p_y,$$

$$\dot{z} = c_4 + \frac{1}{2}y^2,$$

$$\dot{p}_y = -y\left(c_4 + \frac{1}{2}y^2\right) - \xi_\parallel(I_2 - \xi_\perp z + \xi_\parallel y),$$

$$\dot{c}_4 = \xi_\perp(I_2 - \xi_\perp z + \xi_\parallel y) + \epsilon, \quad (10)$$

and these equations are equivalent to the original equations of motion. By working with the variables  $(y, p_y)$  and  $(z, c_4)$ , one need not explicitly consider the equation of motion (2) for the variable  $x$ .

### 3 NUMERICAL SIMULATIONS

This section presents numerical simulations of the orbits of the particles, in three characteristic cases: (i) solar flare RCSs without shear ( $\xi_{\perp} = 10^{-3}$ ,  $\xi_{\parallel} = 0$ ,  $\epsilon = 10^{-5}$ ); (ii) solar flares with a moderate shear ( $\xi_{\parallel} = 0.1$ ), and (iii) the Earth magnetotail current sheet ( $\xi_{\perp} = 0.05$ ,  $\xi_{\parallel} = 0.2$ ,  $\epsilon = 1.8 \times 10^{-6}$ ). The orbits are calculated by integrating the equations of motion derived by the Hamiltonian equation (9). We also studied the case of a solar flare RCS with strong shear ( $\xi_{\parallel} \simeq 1$ ), but the results are qualitatively very similar to those of the Earth magnetotail.

#### 3.1 Mirror-type and escaping orbits

The first calculation refers to electrons injected from the centre of the sheet ( $y = 0$ ,  $z = 0$ ) with various velocities ( $v$ ) and injection angles ( $\theta$ ) defined by  $\dot{z} = v \cos \theta$  and  $\dot{y} = v \sin \theta$ . The velocity  $v$  is given by  $v = \sqrt{\dot{y}^2 + \dot{z}^2}$ . Since  $\dot{x} = 0$ , the injection angle with respect to the direction of the main magnetic component is  $\phi = 90^\circ$ . As shown below, for  $\xi_{\parallel} \neq 0$ , all the particles injected with negative  $\theta$  are bounced at some negative  $y$  and return to the plane  $y = 0$  with a positive angle  $\theta$ , while in the case  $\xi_{\parallel} = 0$  injection in the two half-planes becomes symmetric. Thus, we shall consider injections only on the half-plane  $\dot{y} > 0$ , i.e.  $0 \leq \theta \leq \pi$ . We shall also consider an upper limit for initial velocities defined by the simultaneous requirement that  $v$  does not exceed a non-relativistic limit ( $v/c \leq 0.1$ ) or a very high tail limit of a thermal distribution ( $v < 10v_{\text{th}}$ ). Thus in solar RCSs we set  $0 \leq v \leq 0.1$ , while in the Earth magnetotail we set  $0 \leq v \leq 0.01$ .

Taking initial conditions for 400 orbits in a grid  $20 \times 20$  on the rectangle of the  $(v, \theta)$  plane defined by the above limits, the orbits are integrated numerically for a time  $t = 10^6$ , which corresponds to a few thousand dynamical periods of oscillations in the  $y$ -axis. An orbit is considered as escaping the sheet if it goes outside the zone  $|y| = 1$ , which defines the physical width of the sheet within the integration time. Otherwise, the orbit is considered as trapped in the sheet.

Figs 3(a), (b) and (c) show the main result for electron orbits for our chosen parameter sets. The points in each panel correspond to the values of  $(v, \theta)$  for which the orbits are trapped in the sheet. The following are observed.

(i) The initial conditions corresponding to trapped orbits are limited within a domain of the space  $(v, \theta)$  defined by a limiting boundary.

(ii) As  $\xi_{\parallel}$  increases, the total area of the trapping domain tends to decrease (compare Fig. 3a with 3b).

(iii) When  $\xi_{\parallel} > 0$ , there is a limiting velocity  $v_{\text{min}}$  such that all particles with  $v < v_{\text{min}}$  escape ( $v_{\text{min}} \simeq 0.02, 0.002$  for Fig. 3b, c respectively). For a large integration time  $t$ , we find that the escaping particles just follow the combined gyromotion and  $\mathbf{E} \times \mathbf{B}$  drift where  $\mathbf{B}$  is the component of the magnetic field outside the sheet.

(iv) For  $v > v_{\text{min}}$  there are trapped particles in the range of angles of injection  $\theta_{\text{min}} \leq \theta \leq \theta_{\text{max}}$ , where the angles  $\theta_{\text{min}}$  and  $\theta_{\text{max}}$  depend in general on  $v$ . Asymptotically, for large  $v$ , these angles tend to constant limits. Typical values for these limits are  $\theta_{\text{min}} \simeq \pi/3$ , and  $\theta_{\text{max}} \simeq \pi$ .

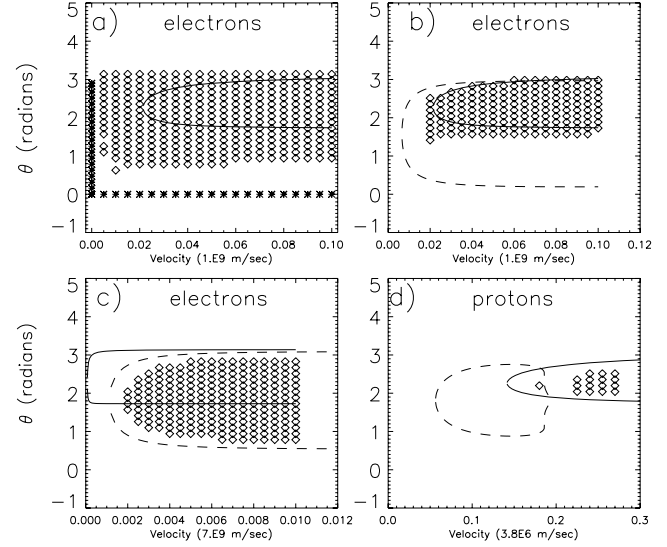


**Figure 3.** The values of initial velocity measure  $|v|$  and angle  $\theta$ , (upwards, with respect to the positive  $z$  semi-axis, for which the orbits of electrons, or protons, injected at  $y = z = 0$ , are trapped in the sheet, for (a)  $\epsilon = 10^{-5}$ ,  $\xi_{\perp} = 10^{-3}$ ,  $\xi_{\parallel} = 0$ , (b)  $\epsilon = 10^{-5}$ ,  $\xi_{\perp} = 10^{-3}$ ,  $\xi_{\parallel} = 10^{-1}$ , (c)  $\epsilon = 1.8 \times 10^{-6}$ ,  $\xi_{\perp} = 0.05$ ,  $\xi_{\parallel} = 0.2$  and (d)  $\epsilon = 3.3 \times 10^{-3}$ ,  $\xi_{\perp} = 0.05$ ,  $\xi_{\parallel} = 0.2$ . Each trapped orbit is represented with a diamond. In panel (a), stars show unstable trapped orbits that escape the sheet when  $y$  is slightly different from zero. The solid and dashed curves represent an analytical determination of the domains of trapping that are valid in the limits  $\xi_{\parallel} \rightarrow 0$  (full line) and  $\xi_{\parallel} \rightarrow 1$  (dashed line) respectively (see Sections 4.2 and 4.3 for details).

Fig. 3(d) shows a similar calculation for protons for parameters relevant to RCS in the Earth magnetotail. We found that, in general, trapping effects are weaker for protons than for electrons. In fact, we did not find trapped protons in solar RCS models for any physically relevant field parameters or proton velocity values. In the case of the geomagnetic tail, the trapping domain for protons has a smaller angle width compared to that of electrons, while trapping requires a larger initial velocity of injection (compare Figs 3c and 3d).

Fig. 4 refers to escaping electrons and protons under the same values of the field components and the same initial conditions of injection within the sheet as in Fig. 3. The final kinetic energy of these particles is plotted against their initial kinetic energy. The main remark here is that, for given initial kinetic energy, there is an upper bound to the amount of possible kinetic energy gain. On the other hand, in Fig. 4(b), (c) and (f) many escaping particles are below the diagonal, meaning that the particles escape by actually losing rather than gaining kinetic energy. The upper dashed line corresponds to a theoretical calculation of the upper bound for the final kinetic energy, as a function of the initial kinetic energy (see Section 4.4). We note also the different behaviour of the kinetic energy gain functions of protons in solar flares and in the Earth magnetotail. In solar flares, the kinetic energy gain for protons can be one order of magnitude larger than their initial kinetic energy (see Fig. 4d and e). However, inside the Earth magnetotail RCS (Fig. 4c and f), the energy gain for protons and electrons are similar functions of the initial kinetic energy. The dimensionless value of the electric field  $\epsilon$ , used in equation (4), is larger than the corresponding value for electrons by a factor  $m_p/m_e$ . This reflects the fact that electric forces, compared to magnetic forces, are relatively more important in protons than in electrons with similar kinetic energy. Consequently, protons are not easily trapped in the sheet.

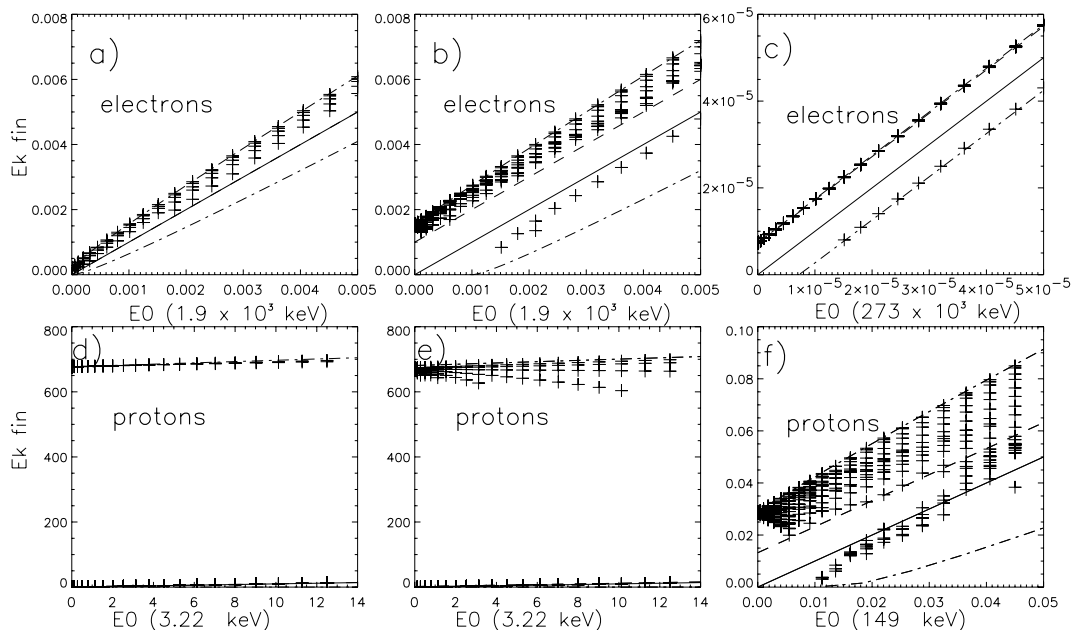


**Figure 4.** Final kinetic energy versus initial kinetic energy for particles in escaping orbits, injected at the centre of the RCS ( $y = z = 0$ ). The physical parameters are: (a)  $\epsilon = 10^{-5}$ ,  $\xi_{\perp} = 10^{-3}$ ,  $\xi_{\parallel} = 0$ ; (b)  $\epsilon = 10^{-5}$ ,  $\xi_{\perp} = 10^{-3}$ ,  $\xi_{\parallel} = 10^{-1}$ ; (c)  $\epsilon = 1.8 \times 10^{-6}$ ,  $\xi_{\perp} = 0.05$ ,  $\xi_{\parallel} = 0.2$ ; (d)  $\epsilon = 1.84 \times 10^{-5}$ ,  $\xi_{\perp} = 10^{-3}$ ,  $\xi_{\parallel} = 0$ ; (e)  $\epsilon = 1.84 \times 10^{-5}$ ,  $\xi_{\perp} = 10^{-3}$ ,  $\xi_{\parallel} = 10^{-1}$  and (f)  $\epsilon = 3.3 \times 10^{-3}$ ,  $\xi_{\perp} = 0.05$ ,  $\xi_{\parallel} = 0.2$ . The upper and lower dot-dashed curves correspond to a theoretical calculation of the maximum kinetic energy gain or loss (equation 30 in Section 4.4, below). The dashed curve in panels (b), (c), (e) and (f) is a calculation of the energy gain by Litvinenko (1996). The energy unit indicated is valid for the energies of both axes of the panel.

The remaining part of this paper is devoted to a theoretical understanding of the above results.

## 4 THEORETICAL ANALYSIS

### 4.1 Visualization of the phase space by Poincaré sections

A theoretical treatment of the orbital dynamics in our model RCS requires illustrating the phase space structure by means of *Poincaré surfaces of sections*. Fig. 5(a) shows a Poincaré section for electron orbits in a solar RCS ( $\xi_{\perp} = 10^{-3}$ ,  $\xi_{\parallel} = 0.1$ ,  $\epsilon = 10^{-5}$  and particles with total energy  $E = 2 \times 10^{-4}$ ). The Poincaré section is computed as follows. For a given orbit, a point is marked on the section every time when the orbit crosses the plane  $y = 0$  with  $\dot{y} > 0$ . As a consequence, from the second equation of (10), we have on the Poincaré section, the equality  $c_4 = \dot{z}$ . All points on this section are restricted in a domain bounded by a closed curve, called the ‘limiting curve’. This curve, derived from equation (9), has the form:

$$\dot{z}^2 + \xi_{\perp}^2 \left( z - \frac{\epsilon}{\xi_{\perp}^2} \right)^2 = 2E + \frac{\epsilon^2}{\xi_{\perp}^2}; \quad (11)$$

in the case of Fig. 5(a),  $E = 2 \times 10^{-4}$ . The form of equation (11) is an ellipse centred at  $(z, \dot{z}) = (\epsilon/\xi_{\perp}^2, 0)$ . The radius of the ellipse increases as the energy  $E$  increases.

Now, a visual inspection of the Poincaré section of Fig. 5(a) reveals that the points lie on a number of open or closed curves. Such curves are called *invariant curves*, and they determine a domain of regular motions on the Poincaré section (domain D in Fig. 5a). In fact, these curves surround a point (B) on the same section, at  $(z_0, \dot{z}_0) \simeq (14.27, -0.009)$ . This point corresponds to a *periodic orbit*, i.e. an orbit which intersects the Poincaré section at the same point at each period. For initial conditions in the neighborhood of

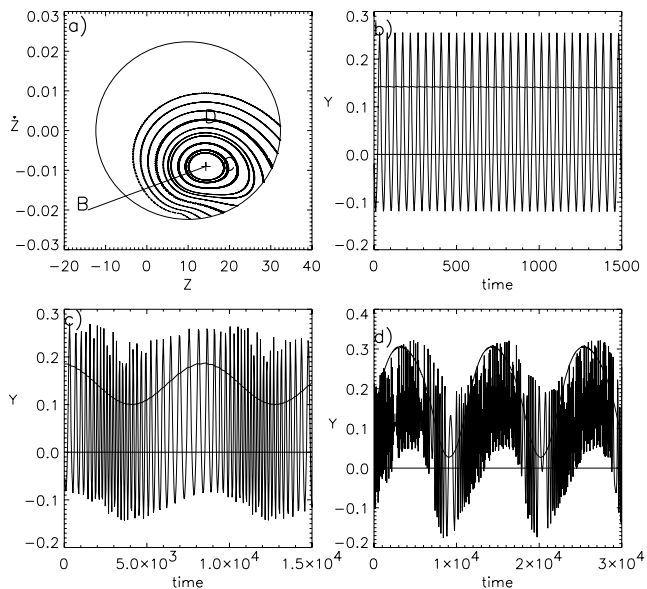


**Figure 5.** Poincaré section  $y = 0$ ,  $\dot{y} > 0$  for orbits in an RCS with  $\xi_{\perp} = 10^{-3}$ ,  $\xi_{\parallel} = 0.1$ ,  $\epsilon = 10^{-5}$  and orbital energy  $E = 2 \times 10^{-4}$ . Panels (b), (c) and (d) show  $y(t)$  (thin line) and  $z(t)$  (thick line) for the orbits with initial conditions marked as B, C, D on the Poincaré section.

$(z_0, \dot{z}_0)$ , quasi-periodic orbits are created. Quasi-periodic orbits intersect the Poincaré section at different points on the same invariant curve. Such curves are also called KAM curves because their existence is predicted by the Kolmogorov (1954), Arnold (1963) and Moser (1962) theorem. In fact, a quasi-periodic orbit lies on a 2D manifold of phase space which is topologically equivalent to a 2D torus. This is called a ‘KAM torus’. The intersection of a KAM torus

with the Poincaré surface of the section  $y = 0$  yields an invariant KAM curve.

The time-evolution of the periodic orbit (B) is shown in Fig. 5(b). The  $y(t)$  coordinate performs a nearly harmonic oscillation, while  $z(t)$  remains practically constant. The closed curve indicated as C on the Poincaré section of Fig. 5(a) corresponds to a quasi-periodic orbit shown in Fig. 5(c). In this case,  $y(t)$  performs an oscillation with frequency nearly equal to the frequency of the periodic orbit. However, the function  $y(t)$  is modulated by a second oscillation which has a much smaller frequency. As shown below, this new oscillation originates from  $z(t)$  which presents the same small frequency oscillation.

In Fig. 5(a) there are also open invariant curves which form arcs that end on the limiting curve. These curves also represent quasi-periodic orbits, as does the one shown in Fig. 5(d). Here,  $y(t)$  performs the same type of oscillations as in the case of Fig. 5(c). However, the amplitude of the second oscillation is now larger so that, for some time-segments,  $y(t)$  does not intersect the  $y$ -axis. These time-segments correspond to a domain  $(z, \dot{z})$  lying outside the limiting curve of the Poincaré section  $y = 0$ .

It is well known from the theory of dynamical systems that, in general, the domain of regular orbits is limited by an outermost KAM curve, while, beyond this curve, orbits are in general chaotic (except perhaps for very small stability islands embedded in a large chaotic domain that are not clearly seen in the present scale). The intersection of a chaotic orbit with the Poincaré section does not lie

on an invariant curve, but it fills stochastically the available space between the last KAM curve and the limiting curve. In fact, we shall see (Section 4.4) that the extensions of the limiting curves to the whole available phase space define the limiting surfaces of motion for constant energy  $E$ . These surfaces are open, allowing particles to escape from the sheet. Since chaotic orbits outside the last KAM torus are free to explore the whole phase space that is energetically available, these orbits always become escaping orbits at a certain time  $t$ .

On the other hand, regular orbits are confined on KAM tori and they perform quasi-periodic oscillations in the  $y$ - and  $z$ -axes. If the oscillation amplitude of  $y(t)$  is smaller than the sheet dimension, particles cannot escape the sheet. However, an escape is possible when the KAM torus for a particular orbit crosses one of the planes of escape  $y = \pm 1$  which define the edges of the sheet in our model.

In summary, escaping orbits can be either chaotic or regular. In the former case, the motion takes place in the domain defined by an inner boundary (a last KAM torus) and an outer boundary (limiting surface of zero velocity). In the latter case, the motion is restricted to a KAM torus and the escape necessarily takes place at some point on this torus, where the torus crosses one of the planes  $y = \pm 1$ .

Fig. 6 shows several characteristic examples of Poincaré sections in our model. Each row of panels in Fig. 6 are computed using the same parameters with each of the panels (a), (b) and (c) in Fig. 3. The columns, from left to right, correspond to increasing orbital energy.

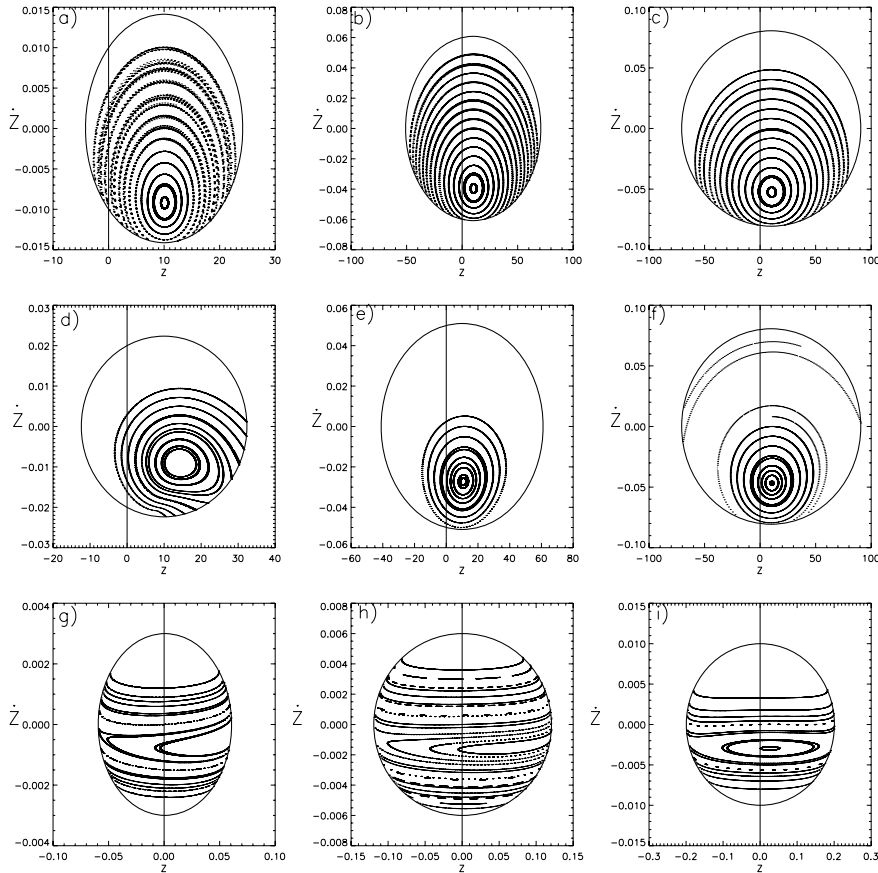


**Figure 6.** Poincaré surfaces of section  $(z, \dot{z})$ ,  $y = 0$ ,  $\dot{y} > 0$ , for the Hamiltonian (9). The parameters are:  $\xi_{\parallel} = 0$ ,  $\xi_{\perp} = 10^{-3}$ ,  $\epsilon = 10^{-5}$  in the first row,  $\xi_{\parallel} = 0.1$ ,  $\xi_{\perp} = 10^{-3}$ ,  $\epsilon = 10^{-5}$  in the second row,  $\xi_{\parallel} = 0.2$ ,  $\xi_{\perp} = 0.05$ ,  $\epsilon = 1.8 \times 10^{-6}$  in the third row. The energy is : (a)  $E = 5 \times 10^{-5}$ ; (b)  $E = 1.8 \times 10^{-3}$ ; (c)  $E = 3.2 \times 10^{-3}$ ; (d)  $E = 2 \times 10^{-4}$ ; (e)  $E = 1.25 \times 10^{-3}$ ; (f)  $E = 3.2 \times 10^{-3}$ ; (g)  $E = 4.5 \times 10^{-6}$ ; (h)  $E = 1.8 \times 10^{-5}$  and (i)  $E = 5 \times 10^{-5}$ .

As the energy increases, the limiting curve occupies a larger area of the Poincaré section (note the different axes limits in the panels of each row, from left to right). Consequently, particles are allowed to have larger velocities and explore larger areas of the phase space.

Fig. 6(a), (b) and (c), referring to a solar RCS without shear, show that the associated phase space is almost entirely filled with invariant KAM curves. These curves surround the fixed point of a periodic orbit, which lies near the lower edge of the limiting curve. The position of the periodic orbit is different in each of the panels (a), (b) and (c), indicating a dependence of the position on the particle energy.

Near the periodic orbit, there are many closed invariant curves. However, further away we observe open invariant curves as well as *zones*, which are similar to curves but with some thickness (mostly visible in Fig. 6a). We shall show (Section 4.5) that these zones correspond to weakly chaotic orbits that behave almost like regular orbits.

Fig. 6(d), (e) and (f) refer to a solar RCS with moderate shear. The periodic orbit still lies near the lower edge of the limiting curve. However, in panel (d), the KAM curves are now clearly distorted from vertical symmetry, and some of them intersect the limiting curve at large values of  $z$ . At higher orbital energy (panels e and f), only closed KAM curves are observed. In fact, the phase space above these curves is filled with many chaotic orbits. Such orbits form *arc segments* on the Poincaré section, as the ones shown in the top of Fig. 6(f). These segments give the impression of being open invariant curves. However, a careful inspection of these curves reveals that the *same* orbit, started on one curve, returns later on a *different* curve of the Poincaré section. In fact, the arc-forming periods are interrupted by periods during which the particle does not cross the Poincaré section at all. Examples of this type can be found in the studies of Chen & Palmadesso (1986), Büchner & Zelenyi (1989), Chen (1992) and in Paper I (for initial conditions at the edge of the sheet).

Finally, in Fig. 6(g), (h) and (j), which correspond to the RCS parameters of the Earth magnetotail, the KAM curves also fill a large part of the available phase space. However, the topological structure of these curves is quite different from that of the previous cases. In particular, most KAM curves are now open and almost horizontal. Closed curves are observed only in the neighbourhood of a central periodic orbit. In panel (g), the centre lies outside the limiting curve, and there are no closed invariant curves. In fact, as shown in Section 4.2, these curves are parts of deformed ellipses with axial ratio very different from unity. Thus, only some parts of the ellipses lie in the domain inside the limiting curve of the Poincaré section.

## 4.2 Theoretical analysis of the phase space structure

The next step in our analysis is to provide a theoretical explanation of the morphology of the regular domain of the Poincaré sections of Fig. 6. In particular, we seek to explain the morphological evolution observed in the pattern of the regular domains as we move through the various panels of this figure.

Without loss of generality (see Paper I), we shall consider the Hamiltonian equation (9) for the choice  $I_2 = 0$ . This Hamiltonian can be written in the form  $H = H_0 + H_{\text{non-linear}}$ , where

$$H_0 = \frac{1}{2} (p_y^2 + c_4^2) + \frac{1}{2} (\xi_{\perp}^2 z^2 + \xi_{\parallel}^2 y^2 + 2\xi_{\perp}\xi_{\parallel}yz) - \epsilon z$$

and

$$H_{\text{non-linear}} = \frac{1}{2} \left( c_4 y^2 + \frac{y^4}{4} \right)$$

The term  $H_{\text{non-linear}}$  can be considered as a perturbation to the term  $H_0$ , thus we shall study first the dynamics induced by  $H_0$ . With a canonical transformation (Paper I)

$$\begin{aligned} u_1 &= \frac{-\xi_{\parallel}y + \xi_{\perp}z}{\sqrt{\xi_{\parallel}^2 + \xi_{\perp}^2}}, \\ p_1 &= \frac{-\xi_{\parallel}p_y + \xi_{\perp}c_4}{\sqrt{\xi_{\parallel}^2 + \xi_{\perp}^2}}, \\ u_2 &= \frac{\xi_{\perp}y + \xi_{\parallel}z}{\sqrt{\xi_{\parallel}^2 + \xi_{\perp}^2}}, \\ p_2 &= \frac{\xi_{\perp}p_y + \xi_{\parallel}c_4}{\sqrt{\xi_{\parallel}^2 + \xi_{\perp}^2}}, \end{aligned} \quad (12)$$

the function  $H_0$  takes the form:

$$H_0 = \frac{1}{2} (p_1^2 + \omega_{10}^2 u_1^2) + \frac{1}{2} p_2^2 - \epsilon \frac{\xi_{\perp}u_1 + \xi_{\parallel}u_2}{\omega_{10}},$$

where  $\omega_{10} = \sqrt{\xi_{\parallel}^2 + \xi_{\perp}^2}$ . We distinguish now two limiting cases as follows.

(i)  $\xi_{\parallel} \rightarrow 0$  (RCS without shear). In this case, the transformation (12) tends to the form:

$$u_1 \simeq z, p_1 \simeq c_4, u_2 \simeq y, p_2 \simeq p_y.$$

Thus the Hamiltonian  $H_0$  implies an oscillation in the  $z$ -axis, with frequency  $\omega_{10}$ , and a free motion in the  $y$ -axis. This is just a Larmor motion with the drift directed towards the  $y$ -axis (see Speiser 1965). This corresponds to the fact that near the plane of reconnection the component  $B_x$  of the magnetic field becomes very small, so that the leading component of the magnetic field is  $\xi_{\perp}$ . Note that the  $\mathbf{E} \times \mathbf{B}$  drift is in the  $x$ -direction, which does not explicitly appear in the analysis because of the Hamiltonian reduction of equation (9). However, away from the plane  $y = 0$ , the component  $B_x$  becomes more important than  $\xi_{\perp}$ . Formally, this is reflected as the effect of the non-linear terms  $H_{\text{non-linear}}$ , which transform the motion in the  $y$ -axis to a mirror type motion, with a small frequency. It can be shown that the second frequency is of the order of  $z_a^2/2$ , where  $z_a$  is the amplitude of oscillation in the  $z$ -axis.

(ii)  $\xi_{\parallel} \gg \xi_{\perp}$ ,  $\xi_{\parallel} \rightarrow 1$  (RCS with large shear). In that case, the normalizing transformation tends to the form

$$u_1 \simeq -y, p_1 \simeq -\dot{y}, u_2 \simeq z, p_2 \simeq c_4.$$

Thus, near the plane of reconnection, the Hamiltonian  $H_0$  now implies a fast oscillation, with frequency  $\omega_{10} \simeq \xi_{\parallel}$  in the  $y$ -axis, and a drift in the  $z$ -axis; that is, the directions of oscillation and drift are reversed with respect to case (i). This is because the main magnetic field component near the plane of reconnection is, now,  $\xi_{\parallel}$ , which is aligned with the  $z$ -axis. The effect of  $H_{\text{non-linear}}$  is, again, to transform the drift motion to a mirror motion on the  $z$ -axis. The frequency  $\omega_2$ , derived from the analysis below, is  $\omega_2 \simeq \xi_{\perp}y_a/(\xi_{\parallel}\sqrt{2})$ , where  $y_a$  is the amplitude of oscillations in the  $y$ -axis.

In order to construct an analytical theory for these limiting cases, we use the theory of *normal forms* (see Paper I for details). In the case of the Hamiltonian (9) there are two perturbing parameters in the problem: (1) the relative importance of the sheared field component [ $\xi_{\parallel} \rightarrow 0$  in case (i) and  $\xi_{\perp}/\xi_{\parallel} \ll 1$  in case (ii)], and (2) the electric field  $\epsilon$ . In order to obtain a useful expression in normal form, we consider first the case without the electric field (i.e.  $\epsilon = 0$  in equation 9). The so-derived Hamiltonian can be written in new canonical variables that clearly unravel the two main oscillations.

The new expression for the Hamiltonian is given as series in new canonical variables  $J'_1$ ,  $u'_2$  and  $p'_2$  (Paper I)

$$Z = \omega_{10}J'_1 + \frac{1}{2} [p_2'^2 + \omega_2^2(J'_1)u_2'^2] + b(J'_1) - c(J'_1)u_2'^4 + \dots \quad (13)$$

where  $\omega_2^2 = (\xi_\perp^2 J'_1 / \omega_{10}^3) + (\xi_\perp^2 J_1'^2 / 8\omega_{10}^8) (25\xi_\perp^2 - 8\xi_\parallel^2) + \dots$ , and  $b(J'_1)$ ,  $c(J'_1)$  are terms of small size defined in Paper I. The variables  $J'_1$ ,  $u'_2$  and  $p'_2$  are near-identity transformations of the variables  $J_1$ ,  $u_2$  and  $p_2$ , where  $J_1$  is the action variable of the conjugate pair  $(J_1, \phi_1)$  defined by  $u_1 = \sqrt{2J_1/\omega_{10}} \cos 2\phi_1$ ,  $p_1 = \sqrt{2\omega_{10}J_1} \sin 2\phi_1$  (see Paper I for details). We notice in particular the relation

$$p'_2 = p_2 + \frac{\xi_\parallel^3 J_1}{2(\xi_\parallel^2 + \xi_\perp^2)^2} + \dots \quad (14)$$

used in the analysis below.

Since no angle conjugate to  $J'_1$  appears in the transformed Hamiltonian, the transformed action  $J'_1$  represents an approximate *integral of motion* of the Hamiltonian  $Z$ . This integral differs from the usual adiabatic invariant in higher order terms in the action variables (see Contopoulos 1966 for a comparison of formal integrals and adiabatic invariants). It is known that such approximate integrals are valid only for regular orbits laying on the surface of invariant KAM tori. The mirror frequency associated with regular orbits of this type is  $\omega_2(J'_1)$ .

Considering now a non-zero electric field,  $\epsilon \neq 0$ , the normal form analysis above is, formally, no longer valid. However, we found that the two limiting cases,  $\xi_\parallel \rightarrow 0$  and  $\xi_\parallel \rightarrow 1$ , can be treated analytically by an appropriate ansatz added to the normal form description. This allows us to calculate theoretically the form of the invariant curves on the Poincaré surface of the section as follows.

#### 4.2.1 Case i: $\xi_\parallel \rightarrow 0$

When  $\xi_\parallel \rightarrow 0$ , the variables  $u_2 \simeq y$  and  $p_2 \simeq p_y$  correspond to an oscillation along the  $y$ -axis with frequency  $\omega_2$ , whereas  $J_1$  corresponds to the action integral of an oscillation along the  $z$ -axis with amplitude  $z_a$  given by  $z_a = \sqrt{2J_1/\xi_\perp}$ . For the cases studied in Fig. 6(a), (b) and (c), one finds that  $\omega_2$  in equation (13) typically satisfies the condition  $\omega_2 \gg \omega_{10}$ , namely, the oscillation in the  $y$ -axis is faster than that of the  $z$ -axis. Thus, an expression for the invariant curves can be found by applying an *averaging technique* in the original Hamiltonian, known in celestial mechanics as ‘Hadjidemetriou mapping’ (Hadjidemetriou 1991). This method produces a ‘*symplectic*’ mapping model for the Poincaré surface of a section of the Hamiltonian system. The final mapping (Appendix A) reads

$$\begin{aligned} \dot{z}_{n+1} &= \dot{z}_n - T\xi_\perp^2 z_n + T\epsilon \\ z_{n+1} &= z_n + T\dot{z}_{n+1} + T\frac{y_a^2}{4}. \end{aligned} \quad (15)$$

The position of the periodic orbit on the Poincaré section is approximated by the period-one fixed point of the mapping (A6), given by

$$z_0 = \frac{\epsilon}{\xi_\perp^2}, \quad \dot{z}_0 = T\epsilon - \frac{y_a^2}{4}. \quad (16)$$

For the fixed point (16), the Hénon’s stability index (Hénon 1965) is equal to  $b = 1 - T^2\xi_\perp^2/2$ . Because  $T \sim 2\pi/\omega_2$ , we have  $T^2\xi_\perp^2/2 \ll 1$ , or  $|b| < 1$ , that is, the central periodic orbit is stable. This

means that the point is surrounded by invariant curves. We readily find the form of these curves:

$$\Phi(\Delta z, \Delta \dot{z}) = \Delta \dot{z}^2 - T\xi_\perp^2 \Delta \dot{z} \Delta z + \xi_\perp^2 \Delta z^2, \quad (17)$$

where  $\Delta z = z - z_0$ ,  $\Delta \dot{z} = \dot{z} - \dot{z}_0$  and  $\Phi = \text{constant}$ . The small non-diagonal term  $T\xi_\perp^2 \Delta \dot{z} \Delta z$  is an artifact of the method that produces the mapping and shall be ignored below; we consider the form of the invariant curves being given by

$$\Phi(\Delta z, \Delta \dot{z}) = \Delta \dot{z}^2 + \xi_\perp^2 \Delta z^2 = \text{constant}. \quad (18)$$

Fig. 7(a) shows a theoretical calculation of invariant curves according to equation (18), for same parameter values as in Fig. 6(b) (shown also as Fig. 7b for comparison). The agreement between these curves is good. However, as stressed above, the real invariant curves have in general a limit defined by an outermost invariant curve, while, beyond this curve, the real Poincaré section is filled with chaotic orbits. This limit cannot be found by equation (18), which gives only the form of theoretical invariant curves. We shall discuss this limit below (Section 4.3).

#### 4.2.2 Case ii: $\xi_\parallel \gg \xi_\perp$ , $\xi_\parallel \rightarrow 1$

At the second limit,  $\xi_\parallel \gg \xi_\perp$ ,  $\xi_\parallel \rightarrow 1$ , the action  $J_1$  corresponds to an oscillation on the  $y$ -axis, while  $u_2 \simeq z$  and  $p_2 \simeq c_4$ . Thus, the expression of the normal form (13) can be used directly to derive the form of the invariant curves of the section  $(z, \dot{z})$ .

Neglecting the small terms  $b(J'_1)$  and  $c(J'_1)$ , the ansatz is now to introduce a term  $\epsilon z \simeq \epsilon u_2'$  for the electric potential in the normal form (13). The new function is

$$Z \equiv E = \omega_{10}J'_1 + \frac{1}{2} [p_2'^2 + \omega_2^2(J'_1)u_2'^2] - \epsilon u_2' \quad (19)$$

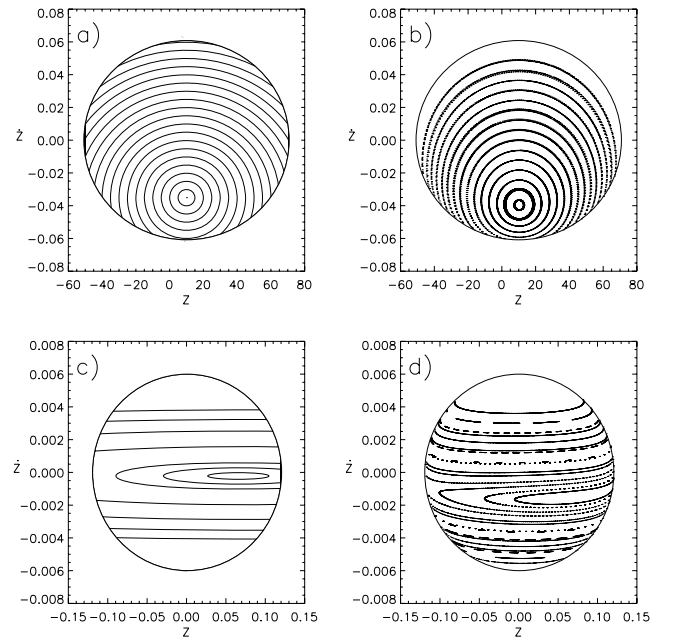


**Figure 7.** Comparison between analytical calculation of Poincaré sections with numerical calculation. (a) Analytical calculation of invariant curves, based on the Hadjidemetriou mapping, holding when  $\xi_\parallel \rightarrow 0$  (see Section 4.2.1). (b) Same as Fig. 6(b). (c) Analytical calculation of invariant curves based on the normal form (see Section 4.2.2). (d) Same as Fig. 6(i).



We also have  $\Delta z_a = \sqrt{2E_2/\omega_2^2}$ , with  $E_2$ , the energy of the mirror oscillation, being related to the total energy via:

$$E = E_1 + E_2 - \frac{\epsilon^2}{2\omega_2^2(J_1')} \quad (25)$$

In the actual calculation, we fix the initial injection velocity  $v_0$ , and vary the injection angle  $\theta$  until we reach the limits where condition (23) is violated.

#### 4.3.3 Comparison of theoretical and numerical results

The above two independent theoretical determinations of the trapping domain are represented in Fig. 3 by a solid curve (for case i) and a dashed one (for case ii). In Fig. 3(a), where  $\xi_{\parallel} = 0$ , the solid curve includes only a part of the real trapping domain. This phenomenon is due to the presence of ‘sticky’ chaotic orbits and will be analysed in Section 4.5. On the other hand, in all other panels of Fig. 3, one of the two theoretical approximations provides a successful representation of the real trapping domain.

In Fig. 3(b), the solid line corresponding to the limit  $\xi_{\parallel} \rightarrow 0$  describes the trapping domain well, especially for high angles near the edge  $\theta = \pi$ . The estimation of the low energy edge of the trapping domain ( $v \simeq 0.02$  in Fig. 3b) is not exact because the KAM curves deviate from the shape of an ellipse at low velocities (compare Fig. 6d and e). Figs 3(c) and (d) refer to the Earth magnetotail for electrons and protons, respectively. The ratio  $\xi_{\parallel}/\xi_{\perp} = 4$  holds for both cases. However, the different values of the scaled electric field ( $\epsilon = 1.68 \times 10^{-6}$  and  $\epsilon = 3.3 \times 10^{-3}$ , respectively), as well as the different velocity range, cause a different approximation to be valid for electrons and protons. Electrons, in a strong magnetic field ( $=\xi_{\parallel}$ ) have gyroradii which are small compared to the sheet thickness. Thus electrons follow guiding centre orbits, i.e. they are better represented by the lowest order terms of approximation (ii). On the contrary, protons have large gyroradii and feel the non-linear effects of the magnetic field variation throughout the sheet. Thus, trapped proton orbits are better represented by the theoretical approximation (i).

#### 4.4 Theoretical determination of the kinetic energy gain for escaping particles

Having analyzed the orbits of trapped particles, we now focus on escaping ones and provide theoretical estimates of their kinetic energy gain when they leave the sheet. This is done as a function of the initial kinetic energy of the particles and of the physical parameters of the sheet.

Limits of motion for non-trapped particles are imposed only by the constant energy condition of an orbit. For a given energy  $E$  the limiting surfaces of zero velocity are given by the conic sections

$$\xi_{\parallel}^2 y^2 + \xi_{\perp}^2 z^2 - 2\xi_{\parallel}\xi_{\perp}yz - 2\epsilon z = 2E. \quad (26)$$

For  $\xi_{\parallel} \neq 0$ ,  $E > 0$ , equation (26) is a parabola (see Fig. 9), which tends to two parallel straight lines as  $\xi_{\parallel} \rightarrow 0$ . For  $\xi_{\parallel} = 0$ , the parabola is open on one half-plane  $y > 0$ , while it closes on the opposite half-plane at the point

$$y_{s,\min} = -\frac{\epsilon}{2\xi_{\parallel}\xi_{\perp}} - \frac{E\xi_{\perp}}{\epsilon\xi_{\parallel}}. \quad (27)$$

This point moves away from the sheet plane as the particle energy increases. As long as  $y_{s,\min} > -1$ , particles can escape only from the one open half-plane, while particles with  $\dot{y} < 0$  at  $y = 0$  are bounced at some point of the half-plane  $y < 0$  and return to the

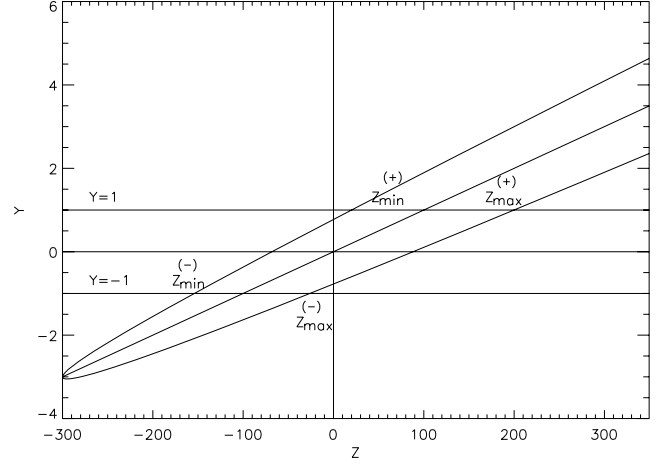


**Figure 9.** The zero-velocity surface is shown to be a parabola. Particles can escape the sheet in different ranges of  $Z$ , depending if they escape from  $y = 1$  or  $y = -1$ . In this example  $\xi_{\parallel} = 0.1$ ,  $\xi_{\perp} = 10^{-3}$ ,  $\epsilon = 10^{-5}$  and the energy of the particles  $E = 0.003$  (see Fig. 4b, where the same parameters are used).

half-plane  $y > 0$ . However, when  $\xi_{\parallel} = 0$  or  $y_{s,\min} < -1$ , particles can escape from both edges of the sheet.

Fig. 9 shows the form of the zero velocity boundary for a case where  $y_{s,\min} < -1$ . Particles can leave the sheet at both edges  $y \pm 1$ . However, the corresponding acceleration lengths are quite different. Namely, the interval  $[z_{\min}^{(+)}, z_{\max}^{(+)})$  (top edge) is shifted by a positive amount, while  $[z_{\min}^{(-)}, z_{\max}^{(-)}]$  is shifted by a negative amount with respect to the symmetry axis  $z = 0$ . Practically, a particle leaving the sheet at  $y = 1$  has a large chance to gain kinetic energy with respect to its kinetic energy of injection at  $y = 0$ . On the contrary, a particle leaving the sheet at  $y = -1$  has a large chance to lose kinetic energy. Particles leaving the sheet at a point tangential to zero velocity curve have the largest possible kinetic energy gain. This is because ‘zero-velocity’ means the  $y$ - and  $z$ -components of the velocity, while the kinetic energy gain is in the  $x$ -velocity component which does not appear explicitly in the reduced equations of motion. The minimum and maximum acceleration lengths for  $y = 1$  are given by

$$z_{\min,\max}^{(+)} = \frac{\xi_{\parallel}\xi_{\perp} + \epsilon \pm \sqrt{2\epsilon\xi_{\parallel}\xi_{\perp} + \epsilon^2 + 2\xi_{\perp}^2 E}}{\xi_{\perp}^2}, \quad (28)$$

while for  $y = -1$ :

$$z_{\min,\max}^{(-)} = \frac{-\xi_{\parallel}\xi_{\perp} + \epsilon \pm \sqrt{-2\epsilon\xi_{\parallel}\xi_{\perp} + \epsilon^2 + 2\xi_{\perp}^2 E}}{\xi_{\perp}^2}. \quad (29)$$

Independently of the details of an orbit, the maximum kinetic energy gain, as a function of the initial kinetic energy  $E_0$ , is calculated by setting the maximum acceleration length equal to  $z_{\max}$ , and  $E = E_0$ . This yields

$$\Delta E_{\max} = \epsilon z_{\max}^{(+)} = \frac{\epsilon}{\xi_{\perp}^2} \left( \xi_{\parallel}\xi_{\perp} + \epsilon + \sqrt{2\epsilon\xi_{\parallel}\xi_{\perp} + \epsilon^2 + 2\xi_{\perp}^2 E_0} \right). \quad (30)$$

In the same way, using the possibilities of equations (28) and (29) one can compute the minimum or maximum kinetic energy gains for particles leaving the sheet from  $y = \pm 1$ . In view of equation (27), an escape from the boundary  $y = -1$  is possible when  $E_0$  satisfies the condition

$$E_0 \geq \frac{\epsilon\xi_{\parallel}}{\xi_{\perp}} \left( 1 - \frac{\epsilon}{2\xi_{\parallel}\xi_{\perp}} \right). \quad (31)$$

Thus, the maximum kinetic energy gain  $\Delta E_{\max}$  is a negative number if  $\xi_{\parallel}\xi_{\perp} > \epsilon$  and

$$E_0 < \frac{\xi_{\parallel}^2}{2}, \quad (32)$$

meaning that a particle with initial kinetic energy below the value (32) leaves the sheet by actually losing kinetic energy.

These theoretical limits are drawn in Fig. 4(a) to (f). In all cases, we find that the curves  $E_0 + \epsilon z_{\max}^{(+)}$  and  $E_0 + \epsilon z_{\min}^{(+)}$  correspond precisely to the orbits with the larger or smaller kinetic energy gain. However, the spreading of the distribution of the particles between these two limits strongly depends on the regular or chaotic character of the orbits. In particular, the spreading is larger when the orbits are chaotic.

#### 4.5 Chaotic sticky orbits

As a final step, we explain the inconsistency of the theoretically derived trapping domain in Fig. 3(a) with the numerically computed domain. As already pointed out in Section 4.1, the discrepancy should be attributed to the presence of chaotic orbits that stay inside the sheet [ $|y(t)| < 1$ ] for a very long time, while they lie outside the domain of the last KAM torus. Such orbits are called ‘sticky orbits’, and they produce arcs with a certain thickness in the Poincaré section. Examples of such arcs were given in Fig. 6.

In order to demonstrate that these apparently trapped orbits are in fact chaotic, we calculate the Lyapunov characteristic number (Benettin, Galgani & Strelcyn 1976)

$$L = \lim_{t \rightarrow \infty, d(0) \rightarrow 0} \frac{1}{t} \ln \frac{d(t)}{d(0)} \quad (33)$$

where  $d(t)$  is the time-evolution of the distance, in phase space, between two neighboring orbits,  $d(0)$  being their distance at  $t = 0$ . The Lyapunov characteristic number (LCN) is equal to zero for regular orbits while it tends to a constant positive value for chaotic orbits. This implies that the deviations  $d(t)$  of chaotic orbits grow with time exponentially, whereas the deviations of regular orbits grow with time algebraically. Lyapunov characteristic numbers of orbits in X-type RCSs were computed, e.g. by Hannah, Fletcher & Hendry (2002) and Martin (1984).

In practice, the Lyapunov number has to be computed for a time that is large enough to allow the quantity  $\ln |d(t)/d(0)|$  to reach its final asymptotic behaviour given by equation (33). In Fig. 10 we show the Lyapunov number evolution for two orbits with initial conditions corresponding to different domains of Fig. 3(a). Both orbits have initial velocity  $v_0 = 0.07$  and  $z_0 = y_0 = 0$ . The first orbit is taken at an initial angle  $\theta = 1$  which corresponds to  $\dot{z} = 3.8 \times 10^{-2}$  and lies outside the domain of trapping as determined theoretically. The second orbit is taken at  $\theta = 2$  which corresponds to  $\dot{z} = -2.9 \times 10^{-2}$  and lies inside the theoretical domain. Fig. 10 shows the Lyapunov number of the first orbit to decrease with time until it reaches a constant value after a time  $\simeq 6 \times 10^4$ . This behaviour is typical of a chaotic orbit. On the contrary, the Lyapunov number of the second orbit decreases with time and it falls asymptotically as  $L \propto t^{-1}$ , indicating that the orbit is regular. We have investigated all the orbits of Fig. 3(a) by using a variant of the LCN method (alignment index, Skokos 2001; Voglis, Kalapotharakos & Stavropoulos 2002), which provides a clear separation of regular and chaotic orbits. The result is shown in Fig. 11. Chaotic orbits are indicated with crosses and regular orbits with diamonds. Clearly, the analytical solution derived in Section 4.3.1 contains all the regular orbits of Fig. 11. On the other hand, the orbits shown by crosses are chaotic, despite the fact that these orbits ‘stick’ to the sheet for quite long times.

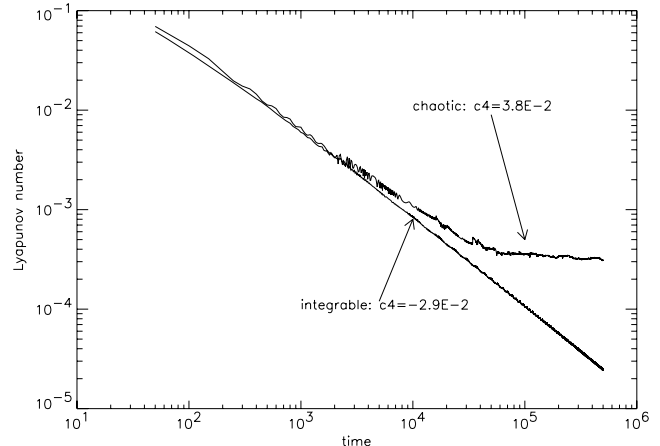


**Figure 10.** Lyapunov number in function of time for two different orbits. For both of them the parameters are  $\xi_{\parallel} = 0$ ,  $\xi_{\perp} = 10^{-3}$ ,  $\epsilon = 10^{-5}$  and the energy is  $E = 2.45 \times 10^{-3}$ , which corresponds to an initial velocity of 0.07. For the first, the Lyapunov number evolves as  $t^{-1}$  and is represented by a straight line on this logarithmic diagram. For the second orbit, the Lyapunov number is stabilized to a constant value, indicating a chaotic behaviour.

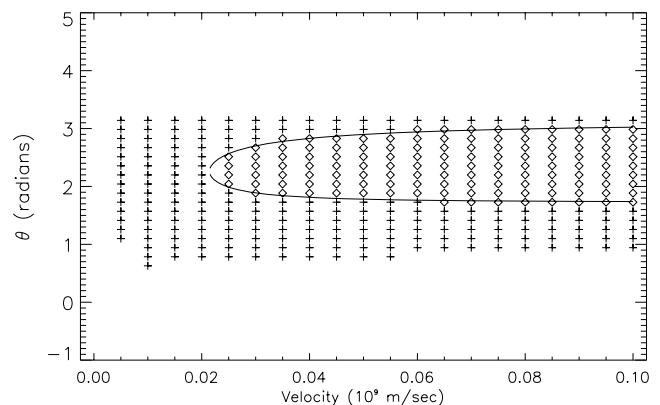


**Figure 11.** Same figure as panel (a) of Fig. 3. There, chaotic orbits are represented with a cross whereas integrable ones with diamonds. The analytical solution separated the two types of orbits exactly.

## 5 SUMMARY AND CONCLUSIONS

In this paper we consider a Harris-type current sheet model with field values relevant to RCSs in the solar atmosphere and in the Earth magnetotail. We then study particle orbits in this current sheet, when the initial conditions of the orbits are taken in the *interior* of the sheet. Our conclusions are as follows.

(1) Numerical simulations show the presence of orbits trapped in a mirror motion within the sheet even when the electric field has large values. Such orbits perform a mirror-type motion with frequencies  $\omega_1 \simeq \sqrt{\xi_{\parallel}^2 + \xi_{\perp}^2}$  and  $\omega_2$  determined by an analytical calculation, based on *normal forms* (Section 4.2). The same theory yields an approximate second integral of motion that is preserved by regular orbits.

(2) We illustrate the phase-space dynamics by computing Poincaré surfaces of section. Such sections provide a clear separation of the domains of trapping (defined by an outermost invariant KAM torus) and of escapes. The boundary of these domains are estimated theoretically by two independent approximations. The

extent of applicability of each approximation is found by comparison with numerical simulations.

(3) In the limit of strong shear ( $\xi_{\parallel} \rightarrow 1$ ), the action integral  $J'_1$  found in our calculation tends to the form of an adiabatic invariant. This integral is better preserved when the length scale of the magnetic field variation is larger than the Larmor radius of particles' orbits, i.e. for  $\xi_{\parallel} \rightarrow 1$  and/or small particles' velocities. When these conditions hold, the phase-space of motion is almost entirely filled with invariant KAM tori (e.g. as in the Poincaré surfaces of Fig. 6g, h and i). On the other hand, an increase of the kinetic energy of the particles causes larger areas of chaotic motions on the Poincaré surfaces (e.g. Fig. 6d, e and f). The extent of the area of regular motion for different RCS parameters and the energies of the particles is explored by analytical means.

(4) Escaping orbits are either regular or chaotic. When the shear ( $\xi_{\parallel}$ ) is non-zero, escapes preferentially follow one of the half-planes determined by the sheet reversal line. Escapes from the other half-plane are possible only when the initial kinetic energy of injection is larger than a threshold value (equation 31). Furthermore, escapes from the preferential plane lead, in general, to a gain of kinetic energy, while escapes from the non-preferential plane lead, in general, to a loss of kinetic energy. Analytical formulae are derived which provide the limits of kinetic energy gain (positive or negative) in both cases with a good precision.

(5) We find 'sticky' chaotic orbits, which remain trapped in the sheet for very long times, before they finally escape. Such orbits are important because they enhance the population of particles that supports the self-consistency of the sheet.

## ACKNOWLEDGMENTS

This research was supported in part by a research grant of the Academy of Athens. Stimulating discussions with Drs J. Contopoulos and H. C. Dara and Prof L. Vlahos are gratefully acknowledged.

## REFERENCES

- Aschwanden M. J., 2004, *Physics of the Solar Corona*. Springer-Verlag, Berlin
- Anastasiadis A., Vlahos L., Georgoulis M., 1997, *ApJ*, 489, 367
- Anastasiadis A., Gontikakis C., Vilmer N., Vlahos L., 2004, *A&A*, 422, 323
- Arnold V. I., 1963, *Russ. Math. Surv.*, 18, 85
- Arnold V. I., Novikov S. P., 1995, *Encyclopaedia of Mathematical Sciences* Vol. 16, *Dynamical Systems VII*. Springer-Verlag
- Benettin G., Galgani L., Strelcyn J.-M., 1976, *Phys. Rev. A*, 14, 2338
- Bhattacharjee A., 2004, *ARA&A*, 42, 365
- Browning P. K., Vekstein G. E., 2001, *J. Geophys. Res.*, 106, 18677
- Bruhwyler D. L., Zweibel E. G., 1992, *J. Geophys. Res.*, 97, 10825
- Büchner J., Zelenyi L. M., 1989, *J. Geophys. Res.*, 94, 11821
- Büchner J., Zelenyi L. M., 1991, *Adv. Space Res.*, 11, (9)177
- Bulanov S. V., 1980, *Sov. Astron. Lett.*, 6, 206
- Burkhart G. R., Drake J. F., Chen J., 1990, *J. Geophys. Res.*, 95, 18833
- Chen J., 1992, *J. Geophys. Res.*, 97, 15011
- Chen J., Palmadesso P. J., 1986, *J. Geophys. Res.*, 91, 1499
- Contopoulos G., 1966, *J. Math. Phys.*, 7, 783
- Contopoulos G., 2002, *Order and Chaos in Dynamical Astronomy*. Springer-Verlag
- Cowley S. W. H., 1978, *Planet. Space Sci.*, 26, 539
- Dalla S., Browning P. K., 2005, *A&A*, 436, 1103
- Deeg H. J., Borovsky J. E., Duric N., 1991, *Phys. Fluids B*, 3, 2660
- Efthymiopoulos C., Gontikakis C., Anastasiadis A., 2005, *A&A*, 443, 663 (Paper I)
- Fletcher L., Petkaki P., 1997, *Solar Phys.*, 172, 267
- Hadjidemetriou J. D., 1991, in Roy A. E., ed., *Predictability, Stability and Chaos in N-Body Dynamical Systems*. Plenum Press, New York, p. 157

- Hannah I. G., Fletcher L., Hendry M. A., 2002, in Wilson A., ed., *ESA SP-506, Proceedings of the 10th European Solar Physics Meeting*. ESA Publications Division, Noordwijk, p. 295
- Hamilton B., McClements K. G., Fletcher L., Thyagaraja A., 2003, *Solar Phys.*, 214, 339
- Heerikhuisen J., Litvinenko Y. E., Craig I. J. D., 2002, *ApJ*, 566, 512
- Hénon M., 1965, *Ann. Astrophys.*, 28, 992
- Kolmogorov A. N., 1954, *Dokl. Akad. Nauk. SSSR*, 119, 527
- Kliem B., 1994, *ApJS*, 90, 719
- Lee E., Lee D.-Y., Min K. W., Seon J., 2001, *Phys. Plasmas*, 8, 4163
- Litvinenko Y. E., Somov B. V., 1993, *Sol. Phys.*, 146, 127
- Litvinenko Y. E., 1996, *ApJ*, 462, 997
- Martens P. C. H., 1988, *ApJ*, 330, 131
- Martens P. C. H., Young A., 1990, *ApJS*, 73, 333
- Martin R. F., Jr, 1984, *J. Geophys. Res.*, 91, 11985
- Mori K. I., Sakai J. I., Zhao J., 1998, *J. ApJ*, 494, 430
- Moser J., 1962, *Nachr. Acad. Wiss. Göttingen II. Math. Phys. Kl.*, 1
- Moses R. W., Finn J. M., Ling K. M., 1993, *J. Geophys. Res.*, 98, 4013
- Nodes C., Birk G. T., Lesch H., Schopper R., 2003, *Phys. Plasmas*, 10, 835
- Petkaki P., MacKinnon A. L., 1997, *Solar Phys.*, 172, 279
- Priest E. R., Forbes T., 2000, *Magnetic Reconnection, MHD Theory and Applications*. Cambridge Univ. Press, Cambridge
- Somov B. V., 1992, *Physical Processes in Solar Flares*. Kluwer, Dordrecht
- Skokos C., 2001, *J. Phys. A*, 34, 10029
- Speiser T. W., 1965, *J. Geophys. Res.*, 70, 4219
- Speiser T. W., Lyons L. R., 1984, *J. Geophys. Res.*, 89, 147
- Vekstein G. E., Browning P. K., 1997, *Phys. Plasmas*, 4, 2261
- Voglis N., Kalapotharakos C., Stavropoulos G., 2002, *MNRAS*, 337, 619
- Zharkova V., Gordovskyy M., 2004, *ApJ*, 604, 884
- Zharkova V., Gordovskyy M., 2005, *MNRAS*, 356, 1107
- Zhu Z., Parks G., 1993, *J. Geophys. Res.*, 98, 7603

## APPENDIX A: DERIVATION OF A 'SYMPLECTIC' MAPPING

Assuming that the  $y(t)$  motion is a fast oscillation given by

$$y(t) \simeq y_a \sin(\omega_2 t), \quad (\text{A1})$$

where  $y_a$  is the amplitude of the  $y$  oscillation, the Hamiltonian is written as

$$H = \frac{1}{2} \left[ c_4 + \frac{1}{2} y_a^2 \sin^2(\omega_2 t) \right]^2 + \frac{1}{2} [\xi_{\parallel} y_a \sin(\omega_2 t) - \xi_{\perp} z]^2 - \epsilon z. \quad (\text{A2})$$

Taking the average of the above expression over the fast-oscillating trigonometric terms yields the averaged Hamiltonian:

$$\tilde{H} = \frac{1}{2} c_4^2 + \frac{y_a^2}{4} c_4 + \frac{1}{2} \xi_{\perp}^2 z^2 - \epsilon z \quad (\text{A3})$$

A symplectic mapping is produced from the averaged Hamiltonian by the generating function

$$W = z_n c_{4,n+1} + TH(z_n, c_{4,n+1}) \quad (\text{A4})$$

where  $T = 2\pi/\omega_2$ . The mapping is given by the canonical equations

$$z_{n+1} = \frac{\partial W}{\partial c_{4,n+1}}, \quad c_{4,n} = \frac{\partial W}{\partial z_n} \quad (\text{A5})$$

The final mapping reads

$$\begin{aligned} \dot{z}_{n+1} &= \dot{z}_n - T \xi_{\perp}^2 z_n + T \epsilon \\ z_{n+1} &= z_n + T \dot{z}_{n+1} + T \frac{y_a^2}{4} \end{aligned} \quad (\text{A6})$$

where  $c_4 = \dot{z}$  on the Poincaré section.

This paper has been typeset from a  $\text{\TeX}/\text{\LaTeX}$  file prepared by the author.